CrossMark

Detecting the Oscillation and Propagation of the Nascent Dynamic Solar Wind Structure at 2.6 Solar Radii Using Very Long Baseline Interferometry Radio Telescopes

Maoli Ma[1,2] , Guifré Molera Calvés[3] , Giuseppe Cimò[4] , Ming Xiong[5] , Peijia Li[1], Jing Kong[6], Peijin Zhang[7], Jiansen He[8], Lijia Liu[9], Pradyumna Kummamuru[3], Chuanpeng Hou[8] , Jasper Edwards[3], Qinghui Liu[1], Zhong Chen[1,10], Zhanghu Chu[1], De Wu[1,11] , Xu Zhao[1,11], Zhichao Wang[1,11] , Songtao Han[6], Quanquan Zhi[6], Yingkai Liu[6], Jonathan Quick[12], Javier González[13] , Cristina García Miró[13], Mikhail Kharinov[14], Andrey Mikhailov[14] , Alexander Neidhardt[15], Tiziana Venturi[16], Marco Morsiani[16], Giuseppe Maccaferri[16] , Bo Xia[1], Hua Zhang[17], and Longfei Hao[18]

[1] Shanghai Astronomical Observatory, 80 Nandan Road, Shanghai, People's Republic of China; mamaoli@shao.ac.cn
[2] Shanghai Astronomical Observatory, Key Laboratory of Radio Astronomy, Chinese Academy of Sciences, 10 Yuanhua Road, Nanjing, JiangSu 210033, People's Republic of China
[3] University of Tasmania, Private Bag 37, Hobart TAS 7001, Australia; guifre.moleracalves@utas.edu.au
[4] Joint Institute for VLBI ERIC, Oude Hoogeveensedijk 4, 7991 PD Dwingeloo, The Netherlands
[5] National Space Science Center, NO.1 Nanertiao, Zhongguancun, Haidian district, Beijing
[6] Beijing Aerospace Control Center, Beijing, People's Republic of China
[7] Institute of Astronomy and National Astronomical Observatory, Sofia, Bulgaria
[8] School of Earth and Space Sciences, Peking University, Beijing, 100871, People's Republic of China
[9] National Astronomical Observatories, Chinese Academy of Sciences, 20A Datun Road, Chaoyang District, Beijing, People's Republic of China
[10] National Basic Science Data Center, Building No.2, 4, Zhongguancun South 4th Street, Haidian District, Beijing 100190, People's Republic of China
[11] University of Chinese Academy of Sciences, 100049 Beijing People's Republic of China
[12] Hartebeesthoek Radio Astronomy Observatory, PO Box 443, Krugersdorp, South Africa
[13] Centro de Desarrollos Tecnológicos, Observatorio de Yebes, Guadalajara, Spain
[14] Institute of Applied Astronomy of the Russian Academy of Sciences, Kutuzova Embankment 10, St. Petersburg, 191187, Russia
[15] Technical University of Munich, Geodetic Observatory Wettzell, Sackenrieder Str. 25, D-93444 Bad Kötzting, Germany
[16] Istituto di Radioastronomia Via P. Gobetti 101, I-40129 Bologna, Italy
[17] Xinjiang Astronomical Observatory, CAS 150 Science 1-Street, Urumqi, People's Republic of China
[18] Kunming Astronomical Observatory, CAS 150 Science 1-Street, Yunnan, People's Republic of China

Abstract

Probing the solar corona is crucial to study the coronal heating and solar wind acceleration. However, the transient and inhomogeneous solar wind flows carry large-amplitude inherent Alfvén waves and turbulence, which make detection more difficult. We report the oscillation and propagation of the solar wind at 2.6 solar radii (Rs) by observation of China's Tianwen and ESA's Mars Express with radio telescopes. The observations were carried out on 2021 October 9, when one coronal mass ejection (CME) passed across the ray paths of the telescope beams. We obtain the frequency fluctuations (FFs) of the spacecraft signals from each individual telescope. First, we visually identify the drift of the frequency spikes at a high spatial resolution of thousands of kilometers along the projected baselines. They are used as traces to estimate the solar wind velocity. Then we perform the cross-correlation analysis on the time series of FF from different telescopes. The velocity variations of solar wind structure along radial and tangential directions during the CME passage are obtained. The oscillation of tangential velocity confirms the detection of a streamer wave. Moreover, at the tail of the CME, we detect the propagation of an accelerating fast field-aligned density structure indicating the presence of magnetohydrodynamic waves. This study confirms that the ground-station pairs are able to form particular spatial projection baselines with high resolution and sensitivity to study the detailed propagation of the nascent dynamic solar wind structure.

Unified Astronomy Thesaurus concepts: Solar wind (1534); Very long baseline interferometry (1769); Deep space probes (366)

1. Introduction

The process on how the corona is heated to be many hundreds of times hotter than the photosphere and accelerated to form a supersonic stellar wind is still not clear. The observation of the nascent solar wind inside 6 solar radii (Rs) is very valuable to study the acceleration model (Grail et al. 1996; Adhikari et al. 2020). However, the near-Sun solar wind is much more variable and structured, accompanied by the coronal mass ejection (CME), the polar plume, etc. In order to monitor the large-scale solar wind

from 1.5 to 32 Rs, the Solar and Heliospheric Observatory (SOHO) and the onboard Large Angle and Spectrometric Coronagraph (LASCO) instruments were launched in 1995 to the Lagrange L1 to study the solar corona (Brueckner et al. 1995; Domingo et al. 1995). To further study the electromagnetic fields and wave–particle interactions, NASA's Parker Solar Probe (PSP) was launched in 2018 to cross the Alfvén critical surface and orbits at a perihelion of 9 Rs from the solar surface beginning in 2024 (Fox et al. 2016). These observations have improved our understanding about the mechanisms of solar wind acceleration (Bale et al. 2019; He et al. 2021). However, PSP will never probe as close to the Sun as the remote-sensing methods.

The human made spacecraft specially designed for deep space exploration provides an excellent radio source for the

Table 1
Specifications of the Observations on 2021 October 9: Time, the Projected Mars Position, Stations, and Targets

Time	Heliocentric Distance (R_s)	Heliographic Latitude (degree)	Carrington Longitude (degree)	Stations	Targets
UTC 06:50–13:00	2.62	51	258	Hh,Zc,Bd,Mc,Ys	TIW
UTC 06:50–08:30	2.62	51	258	Hh,Zc,Bd,Mc,Ys,Yg	MEX

radio remote-sensing of the solar corona. The spacecraft operates at a high frequency band (GHz) with strong signal-to-noise ratio, which enables the observation of solar wind very close to the Sun during conjunction. Therefore, almost all the interplanetary spacecraft are used to deduce the large-scale coronal structure. Patzold et al. (2012, 2016) measured the total electron content using Mars Express (MEX), Venus Express, and Rosetta. Imamura et al. (2014) derived the radial profile of solar wind outflow speeds between 1.5 and 20.5 Rs from the amplitude fluctuations of the radio signal scintillation in the Akatsuki 2011 observations. Molera Calvés et al. (2017) charactered the coronal mass ejections from the MEX observations. Efimov et al. (2018) inferred the radial acceleration of slow solar wind at low heliolatitudes from two-station frequency fluctuation (FF) measurements of the Galileo spacecraft. Wexler et al. (2019) measured the speed of solar wind by examining the power spectral density of FFs. Wexler et al. (2020) presented a two-component model for interpretation of the FF from the Akatsuki spacecraft and determined the radial profile of slow wind speed in the extended corona using mass-flux continuity. Ma et al. (2021a) measured the radial solar wind velocity within 10 Rs with very long baseline interferometry (VLBI) radio telescopes.

Tianwen-1 (TIW) is the first Chinese spacecraft exploring Mars, entering orbit around Mars on 2021 February 10 (Zhang et al. 2022). Meanwhile, the Mars Express spacecraft is operating in Mars' orbit since early 2004 (Schmidt 2003; Patzold et al. 2016). We conducted the solar conjunction observations of TIW or MEX in 2021 with the radio telescopes from the European VLBI network (EVN) and from the University of Tasmania. In this Letter, we use the recording system of the VLBI network. We do not conduct multiplying interferometer analysis, which is a standard approach for VLBI. Instead, we obtain the FF from each individual telescope, then carry the cross-correlation analysis of the FF from different telescopes to estimate the solar wind velocity. We present the observations and data process in Section 2. Section 3 presents the propagation time and velocity measurements, and Section 4 is the conclusions.

2. Observations and the Data Process

2.1. Observations

The observations were conducted on 2021 October 9, as indicated in Table 1. The projected Mars position in heliographic latitude and Carrington longitude are 51° and 258°, with the heliocentric distance 2.6 Rs from the center of the Sun. TIW and MEX were observed in the same beam by the EVN telescopes of Hartebeesthoek 25 m (Hh), Zelenchukskaya 32 m(Zc), Badary 32 m (Bd), Medicina 32 m (Mc), Yebes 40 m (Ys), and Yarragadee 12 m (Yg) antenna of the University of Tasmania. The observation of TIW continued from 06:50 to 13:00, and MEX ended at 08:30. Due to the limitation of visibility, Mc and Ys participated the observations later at 07:40, and Bd ended earlier at 09:30. The observation covered

the eruption passage typical of a CME. The CME was a halo in SOHO LASCO-C2 and C3. The associated eruption followed the M1.6 class flare from AR 2882 and was characterized by significant dimming: an EUV wave and posteruptive arcades seen mostly to the west from AR 2882 in the Solar Dynamics Observatory Atmospheric Imaging Assembly 193, 304, 171, and in EUVI A 195 starting at 2021-10-09T06:33Z.[19]

The radio telescopes observed the X-band (8.4 GHz) downlink signals from the spacecraft. TIW was working in safe mode with low gain antenna on board and the transponder in noncoherent mode. The equivalent isotropically radiated power of the transmitter on board is only ~26 dBW. The Allan variance of the onboard oscillator is 10^{-12} per second, allowing us to identify the FF caused by the interplanetary scintillation from the equipment noise. MEX was operating in a closed-phase locked loop with one of the antennas of the European Space Agency's tracking stations.

2.2. Measuring the Frequency Fluctuations

We have applied three methods to obtain the time series of the FF of the downlink spacecraft signal. Figure 1 is the power spectral density (PSD) of signals from MEX and TIW at Ys station at 08:30 on October 9. The carrier-to-noise ratio (CNR) is defined as the ratio of the main carrier power to the noise density. The CNR of MEX is about 30 dBHz. Due to the low gain antenna used by TIW, the received signal is extremely weak, less than 10 dBHz, totally obscured by the noise. We use the local correlation method to extract the frequency of the weak signal (Ma et al. 2021b). To mitigate the CNR loss due to frequency smearing caused by Doppler shift, the local correlation method compensates for the Doppler shift of the main carrier with a signal propagation model constructed by the kinematics of the spacecraft and the onboard transmitted frequency. Only the signal that is dynamically similar to the model can be recovered as a detectable one as in Figure 1(III).

The CNR of the signal after the local correlation is about 20 dBHz, enabling the frequency measurements. Since the signal of TIW could not be resolved in the PSD of the raw data, we utilize its CNR after the local correlation in the following pictures for analysis. For the stronger signal of MEX, the CNR in the PSD of the raw data is applied.

Owing to the lacking the transmission frequency information of MEX, we use two other methods instead to process them. The data recorded at the Yg station is processed with the high spectral resolution multitone spacecraft Doppler tracking software developed by Molera Calvés et al. (2021). And we use the instantaneous Doppler frequency method to obtain the received frequency of MEX observed at other EVN telescopes (Zheng et al. 2013). A polynomial fit is applied to the frequency time series to determine the variation tendency, then subtracted from the frequency time series to generate an FF time series about zero. For the residual frequency measured

---
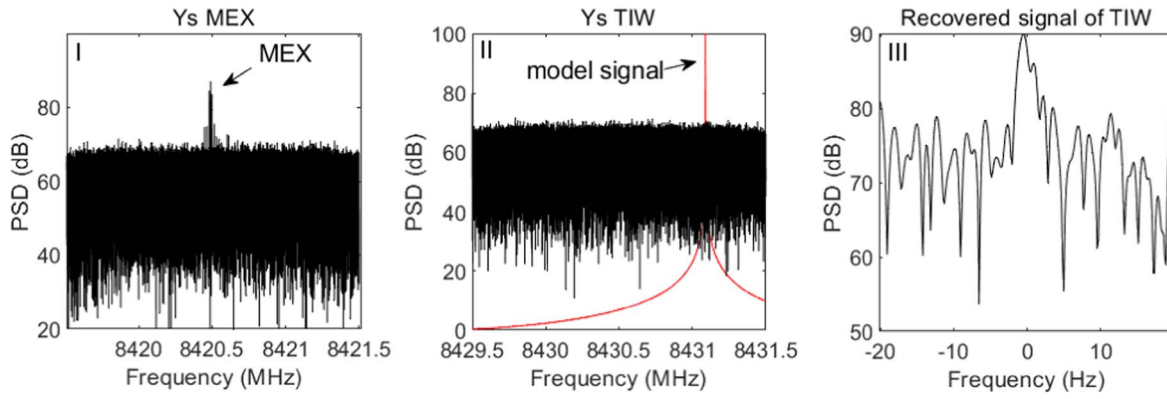
[19] https://kauai.ccmc.gsfc.nasa.govs/DONKI/view/CMEAnalysis/17926/3

Figure 1. Power density spectra (PSD) of Mars Express (MEX) and Tianwen-1 (TIW) at Ys station at 08:30 on October 9. (I) MEX. (II) TIW and the dynamic signal model. The main carrier of TIW is obscured by the noise. (III) Recovering of the signal of TIW with local correlation.

from local correlation, a two-order fit is used (Ma et al. 2021b). For the received frequency of MEX, a six-order fit is used to remove the Doppler shift. Due to the weak signal of TIW, the integration time of the frequency fluctuations is set to 2 s. Figures 2(a) and (b) present the frequency fluctuations and the CNR for TIW and MEX on October 9, respectively. The observations mode for Yg antenna includes observing the target for 19 minutes with a 1 minute break for the repointing and calibration. Some longer data gaps were caused for a switch in operations of the spacecraft between the one to two-way mode. At Yg antenna we only process data in the two-way mode. For other EVN telescopes, we carefully delete the data around the switch time. A detailed analysis on the FF is presented in Section 3.1.

3. Results and Analysis

3.1. The Effect of the Density Inhomogeneities on Spacecraft Signals

The CME entered the LASCO-C2 field of view at 07:09 (Figure 3(I)). The CME front arrived at the projected Mars position around 07:20 and lasted until 07:32 (Figures 3(II) and (III)). It spread out (Figure 3(IV)), and almost faded away after 11:00. The differences in images between 11:00 and 12:00 were not distinguishable (Figure 3(V) and (VI)). In Figure 2, we can see the effects of the CME on both TIW and MEX signals. The FF of the background solar wind is $-1 \sim 1$ Hz. From 07:06, stronger FFs distinctly appear above the background field, and become very severe between 07:20 and 07:32, with the fluctuations up to $-30 \sim 30$ Hz and the CNR decreasing about $5 \sim 8$ dBHz. The effects on signal weaken after 08:00 and fade away after 11:00. Here we call the stronger FF "spikes," which are distinguished because of the density contrast between the transient inhomogeneities and the ambient flow.

The onboard or ground systems could result in some abnormal radio frequency interference (RFI) as well. The simultaneous observations of multiple stations and spacecraft enable us to distinguish the spikes caused by solar plasma from the RFI. Sometimes, the RFIs appear only on one station but not on another. See the frequency jumps appear at 08:37:16 and 08:51:12 only at Mc. We also find an RFI appears at the same time 08:07:23 at Hh, Zc, Bd, Ys, and Mc stations observing MEX; however, we do not see the corresponding RFI from TIW. This RFI is caused likely by some factor on MEX. Those are excluded in the following analysis.

3.2. Measuring the Propagation Time and Velocity of the Solar Wind from Visual Spikes

By inspection of the spikes at different stations, the appearance time of spikes is different. The absolute values of the spikes are larger than the ambient FF. We pick up the typical points (such as the peaks of the spikes) by visual comparison and mark with "∘" to calculate the time lag. In Figure 4(I), a spike appears at Hh at 07:16:20 with the jumping value -6.8 Hz. The recording time for the similar spikes at Bd and Zc is 07:16:24 and 07:16:28, respectively. Their delays relative to Hh are 4 s for Bd-Hh and 8 s for Zc-Hh. In Figure 4(V), the spikes appear from MEX as well as TIW. We prefer to display the spikes from Yg MEX and TIW as a comparison, for they are enough to show the lags. In Figure 4(IV), the spikes with $\sim$30 Hz appear on TIW around 07:30. We also find similar spikes around 07:30 on MEX and do not show these here.

The different occurrence times of the spikes at different stations provide the visual evidence of the drift of the scintillation pattern among the ray paths. By differing the different occurrence times we obtain the propagation time of the inhomogeneities. To study the propagation velocity, we have projected the baselines between the station pairs onto the sky plane in heliographic coordinates, then calculated the components in the radial $\overrightarrow{P_{\mathrm{rad}}}$ and latitudinal $\overrightarrow{P_{\mathrm{tan}}}$ from the Sun (see the Appendix). The time lags, $\overrightarrow{P_{\mathrm{rad}}}$, $\overrightarrow{P_{\mathrm{tan}}}$, and the related velocity v_{rad}, v_{tan} of the spikes between two stations are listed in Table 2. Typically, the time lags between the Hh/Ht or Yg related radial baselines are similar, except two moments of 10:27:12 and 11:52:50. At 10:27:12, we find the indispensable lag difference along the tangential direction, with 12 s, 16 s, and 28 s detected by Mc-Ys, Zc-Mc, and Zc-Ys. The corresponding v_{tan} are 66, 89, and 79 km s^{-1} poleward. At 11:52, the lag between Mc-Zc is 6 s, and v_{tan} is 210 km s^{-1} equatorward. We do not calculate the lag of the Ys related baseline for the spike of Ys is not distinct enough to find the typical point.

The lag and velocity estimation by visual comparison of spikes at different stations can give us a straightforward understanding about the propagation of the solar wind density structures. To depict the velocity variation during the whole observation, we then perform the cross-correlation analysis on the time series of the FF (Ma et al. 2021a).
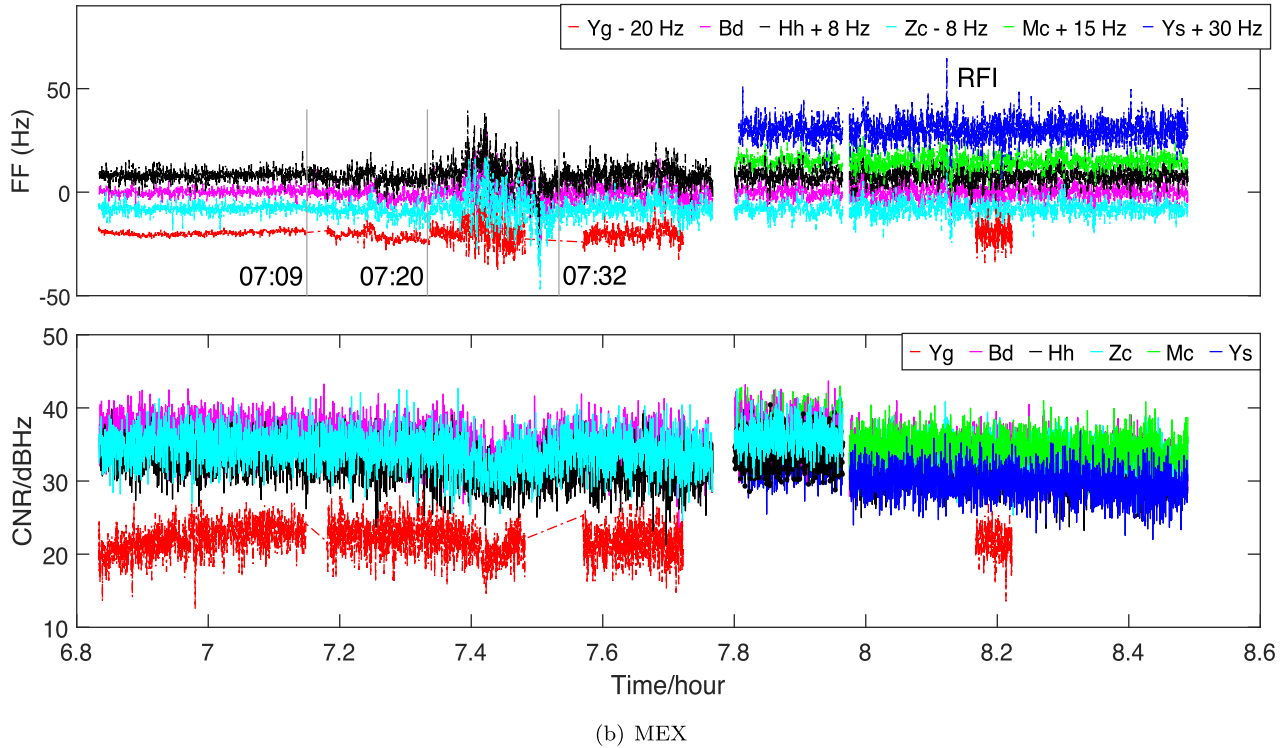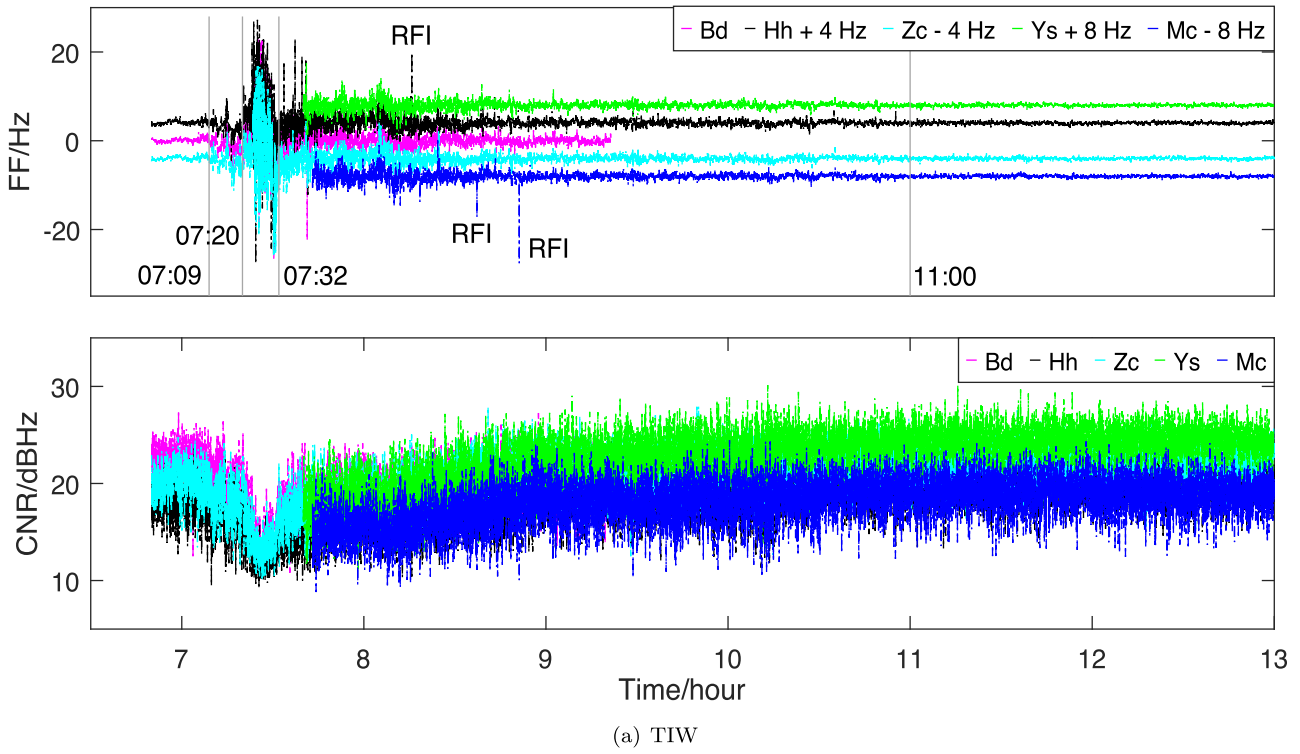
(a) TIW

(b) MEX

Figure 2. The frequency fluctuation (FF) and the carrier-to-noise ratio (CNR) of Tianwen-1 (TIW) (a) and MEX (b) from individual telescopes. The FF is shifted by a constant value given in the legend. The CME entered the LASCO-C2 field of view at 07:09. The CME front arrived the projected Mars position around 07:20. The effects of the CME on the signal weaken after 07:32 and fade away after 11:00. In (a), the frequency jumps appear at 08:37:16 and 08:51:12; only at Mc are the radio frequency interferences (RFIs). In (b), an RFI appears at the same time 08:07:23 from Hh, Zc, Bd, Ys, and Mc stations when observing MEX.

3.3. Measuring the Propagation Time and Velocity of the Solar Wind from Cross Correlation

We divide the FF into 12 continuous time series with a mean duration of 30 minutes, thus, 06:50–07:05, 07:05–07:20, 07:20–07:44, 07:44–08:40, 08:40–09:20, 09:20–10:00, 10:00–10:30, 10:30–11:00, 11:00–11:30, 11:30–12:00, 12:00–12:30, and 12:30–13:00. To balance the scintillation pattern and the instrument noise, the cutoff frequency ν_c is set to 0.05 Hz. It is
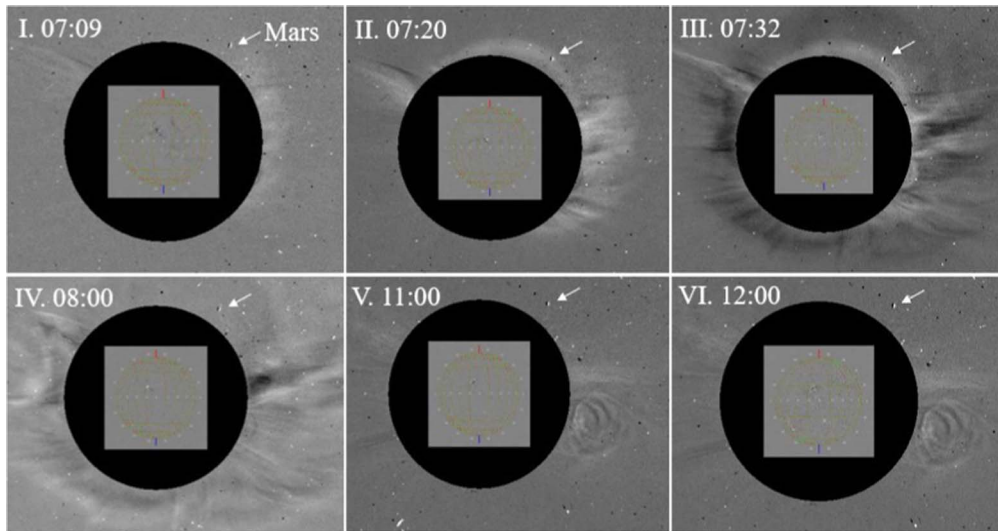
Figure 3. The LASCO pictures. (I) The CME entered the LASCO-C2 field of view at 07:09. ((II)–(III)) The CME front arrived at the projected Mars position. (IV) The CME weakens after 08:00. ((V)–(VI)). The fade away of the CME.
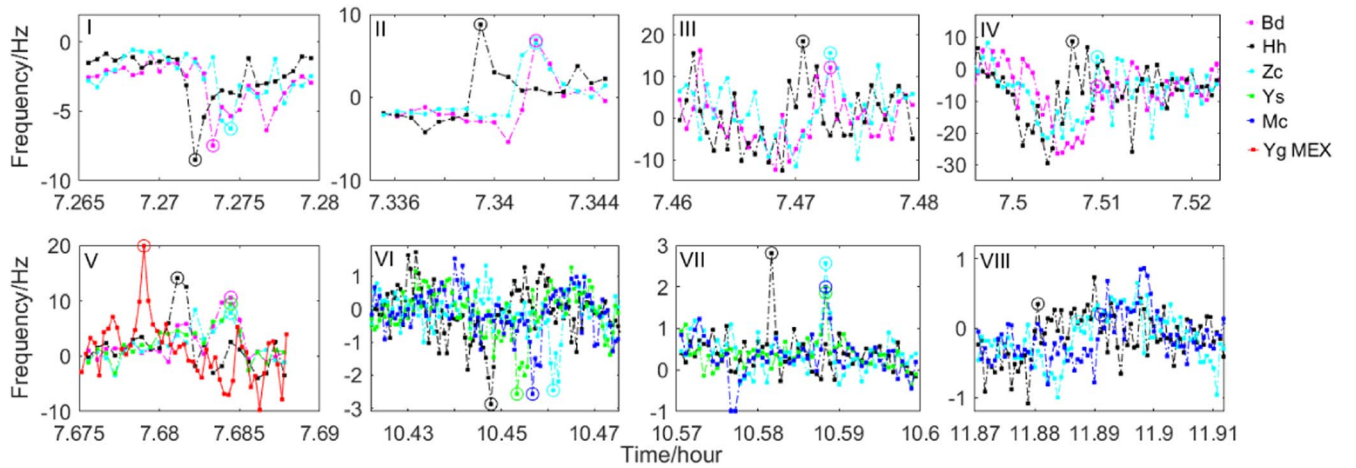

Figure 4. The spikes in frequency fluctuations at different moments from individual telescopes. ((I), (II), (III), and (IV)). Spikes among Hh, Bd, and Zc from TIW. (V) Spikes among Yg from Mars Express (MEX), Hh, Bd, Zc from TIW. ((VI)–(VII)). Spikes among Hh, Zc, Ys, and Mc from TIW. (VIII) Spikes from Hh, Zc, and Mc from TIW.

the most suitable to retain the scintillation from the CME and filter the interferences from instrument noise. In order to improve the resolution of the time lag, we take a two-order polynomial fitting on six points around the peak of the cross-correlation functions (CCFs). Then we obtain the cross-correlation coefficient (CC) and the related lag of the peak from the fit curve. The error of lag is obtained through analyzing the uncertainties of the fit coefficients.

In Figure 5, the CC before the eruption of the CME is below 0.5 on the baselines of Bd-Hh, Zc-Hh, and Zc-Bd. They suddenly rise to 0.9 owing to the eruption of the CME, then gradually decrease with the decline of the CME. The lags on the radial baselines are larger than 8 s, and v_{rad} gradually decelerates from ∼500 to ∼100 km s^{-1}.

After 10:30, accompanying the fading away of the CME, we clearly see the presence of two solar wind streams crossing the lines of sight (LOSs). Figure 6 presents the CCFs of Ys-Hh, Mc-Hh, and Zc-Hh between 10:30 and 13:00. Figure 6(a, II) shows a "bump" with two distinct peaks between 10:30 and 11:00 on Ys-Hh. The main peak with a lag of 25.9 s relates to the "slow stream" corresponding to the CME, and the other with a lag of

6.1 s relates to a "fast stream." After 11:00, the scintillation pattern then is dominated by the fast stream. The CC of the cross-correlation peak relating to the fast stream is up to 0.6 stronger than the CC of the tail of the CME. And the peak relating to the CME almost disappears after 12:00. We also see the interaction of the CME and the fast stream on Mc-Hh (Figure 6(b)). The time lag of the fast stream is between 5.4 ∼ 7.2 s between 11:00 and 13:00, with CC of the peak up to 0.4. We fail to detect the fast stream on the baseline of Zc-Hh (Figure 6(c)). Instead, with the tangential distance of ∼1500 km at Zc-Hh, the scintillation pattern in Figure 6(c, I) includes both the radial and tangential components. The lag of the main peak is 50.0 s, matching with the lag of 48 s measured at 10:26:52 in Table 2. The lag of the second peak is 25.1 s, consistent with the radial components measured at other time series.

The fast streams display an acceleration progress, 725 ∼ 1106 km s^{-1} obtained from Ys-Hh, 626 ∼ 848 km s^{-1} from Mc-Hh. To further verify the fast stream, we try not to use the filter on the FF ($\nu_c = 0$ Hz). The lags from $\nu_c = 0$ Hz at Ys-Hh are consistent with $\nu_c = 0.05$ Hz in the order of 1 s with a CC of ∼0.4. At Mc-Hh, the lags of the fast stream are between 2 ∼ 8 s
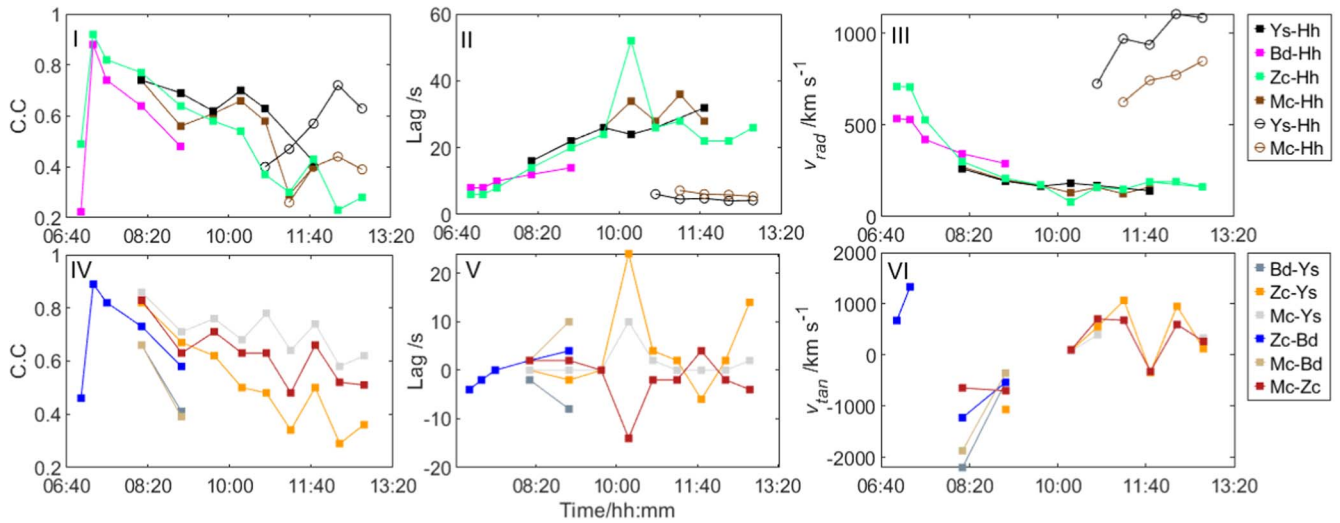
Figure 5. The correlation coefficient, lag, and velocity of the solar wind. The circle plots with Ys-Hh and Mc-Hh relate to the "fast stream." ((I), (II), and (III)) The CC, lag, and velocity along the radial direction. ((IV), (V), and (VI)) The CC, lag, and velocity along the tangential direction.

Table 2
The Lags, Radial Velocity $v_{\rm rad}$ and the Tangential Velocity $v_{\rm tan}$ Measured from the Frequency Spikes

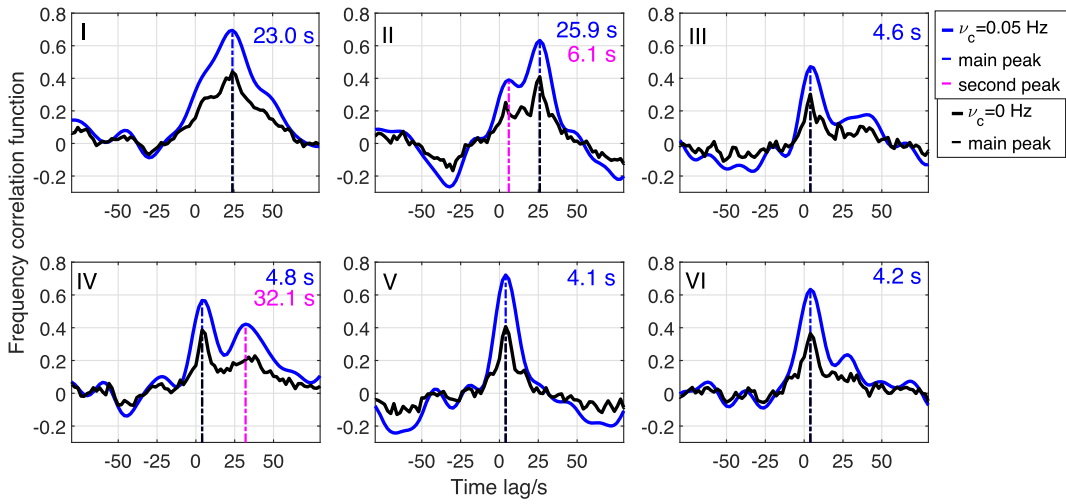| Spikes (Hz)	Time	Time	lag (s)	$P_{\rm rad}$ (km)	$P_{\rm tan}$ (km)	v_{rad} (km s^{-1})	v_{tan} (km s^{-1})
−6.8	Hh 07:16:20	Zc 07:16:28	8	4235	1550	529	/
−6.8	Hh 07:16:20	Bd 07:16:24	4	4218	4212	1054	/
8.1	Hh 07:20:22	Zc 07:20:30	8	4230	1552	528	/
8.1	Hh 07:20:22	Bd 07:20:30	8	4200	4205	525	/
25.2	Hh 07:28:14	Zc 07:28:22	8	4220	1555	527	/
25.2	Hh 07:28:14	Bd 07:28:22	8	4190	4180	523	/
30.8	Hh 07:30:9.5	Zc 07:30:18.5	9	4225	1560	469(MEX)[a]	/
30.8	Hh 07:30:9.5	Bd 07:30:18.5	9	4178	4179	464(MEX)[a]	/
30.8	Hh 07:30:24	Zc 07:30:34	10	4230	1556	423	/
30.8	Hh 07:30:24	Bd 07:30:34	10	4190	4178	419	/
11.9	Hh 07:40:52	Zc 07:41:04	12	4200	1560	350	/
11.9	Hh 07:40:52	Ys 07:41:04	12	4150	−170	345	/
11.9	Hh 07:40:52	Bd 07:41:04	12	4160	4155	346	/
11.9	Yg 07:40:44	Zc 07:41:04	20	4650	−1000	232	/
11.9	Yg 07:40:44	Ys 07:41:04	20	4600	−2500	230	/
11.9	Yg 07:40:44	Bd 07:41:04	20	4590	1500	230	/
−2.5	Hh 10:26:52	Ys 10:27:12	20	4393	−900	219	/
−2.5	Hh 10:26:52	Mc 10:27:24	32	4465	400	139	/
−2.5	Hh 10:26:52	Zc 10:27:40	48	4160	1320	86	/
−2.5	Ys 10:27:12	Mc 10:27:24	12	100	800	/	66
−2.5	Mc 10:27:24	Zc 10:26:40	16	−300	1428	/	89
−2.5	Ys 10:27:12	Zc 10:27:40	28	−200	2221	/	79
2.5	Hh 10:34:54	Zc 10:35:18	24	4160	1200	173	/
2.5	Hh 10:34:54	Ys 10:35:18	24	4416	−905	184	/
2.5	Hh 10:34:54	Mc 10:35:18	24	4475	−120	186	/
0.5	Hh 11:52:50	Zc 11:53:12	22	4200	1000	190	/
0.5	Hh 11:52:50	Mc 11:53:28	30	4550	−200	150	/
0.5	Zc 11:53:12	Mc 11:53:28	6	380	−1258	/	−210

Note.
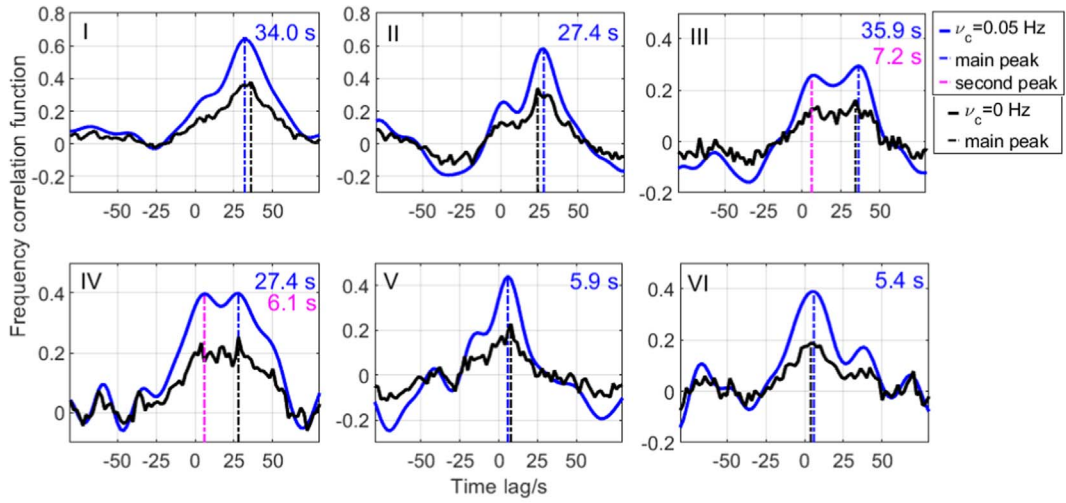[a] This measurement is from the solar conjunction observation of MEX.

with a CC of ∼0.2. It indicates the fast stream propagating better along Ys-Hh.

In Figure 5(VI), the direction of $v_{\rm tan}$ reverses for four times with the evolution of the CME. All baselines indicate the equatorward component between 07:40 and 09:25. The $v_{\rm tan}$
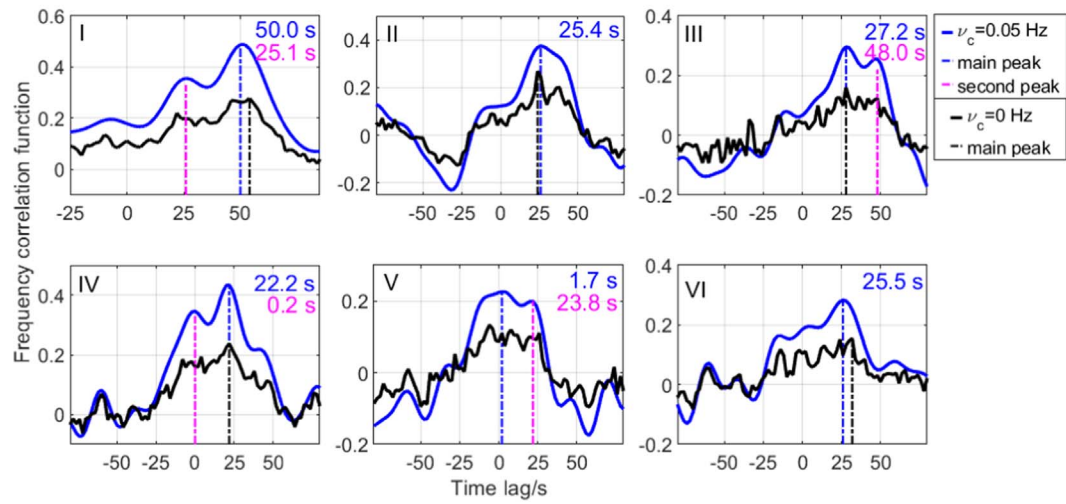
around 09:00 are −350, −532, −532, and −698 km s^{-1} measured from the Mc-Bd, Zc-Bd, Mc-Ys, and Mc-Zc. After 10:00, $v_{\rm tan}$ exhibits elegant large-scale sinusoidal wavelike motions. A definitively poleward component appears between 10:00-10:30 with 102.5, 93, and 79 km s^{-1} measured from Mc-

Figure 6. The cross-correlation function of frequency fluctuations of Hh-Ys (a), Hh-Mc (b), and Hh-Zc (c). (I) 10:00–10:30. (II) 10:30–11:00. (III) 11:00–11:30. (IV) 11:30–12:00. (V) 12:00–12:30. (VI) 12:30–13:00.
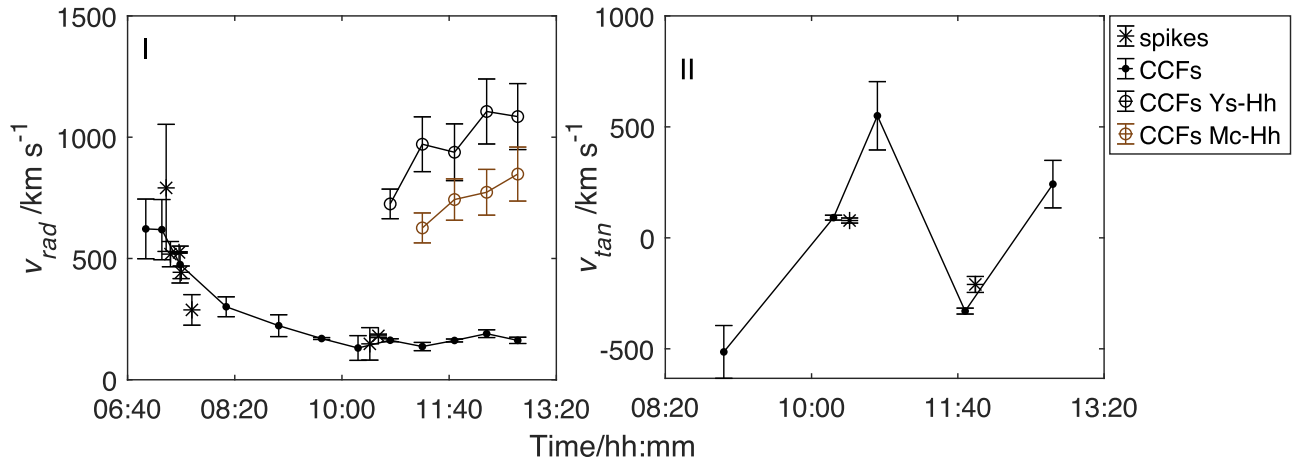
Figure 7. The velocity obtained from the visual spikes and the cross correlation. (I) Radial velocity. (II) Tangential velocity.

Zc, Zc-Ys, and Mc-Ys. Then v_{tan} turns equatorward between 11:30–12:00, and poleward again after 12:00. Two reverses of v_{tan} that happened between 10:00–10:30 and 11:30–12:00 match the measurements from visual spikes in Table 2. The deflection to the north pole of the Sun results in the spikes of -2.5 Hz (redshift) at 10:27 in Figure 4(VI). Another deflection to the ecliptic plane results in the spikes of 0.9 Hz (blueshift) at 11:52 in Figure 4(VIII). These distinct drifting spikes make our measurements of the oscillation more convincing.

3.4. Discussion

The observations from multitelescopes give us an opportunity to evaluate the consistency and rationality of the velocity. We calculate the mean velocity and the standard deviation (STD) at each moment or from the same time series from the different baselines. The error bars are the STD. For the velocity measured from a single baseline, e.g., the field-aligned fast stream, the error bars are calculated from the error of the lag. We give up the v_{tan} from small lags of ± 2 s to avoid the spuriously large measurement errors. For the highly anisotropic fast stream, we display the velocity from both Ys-Hh and Mc-Hh. Finally, the velocity obtained from spikes and cross correlation is presented in Figure 7.

The v_{rad} of the CME front between 07:16 and 07:20 is 643 ± 138 km s^{-1}. When the FFs become the most intense (07:20–07:30), the mean v_{rad} is 480 ± 40 km s^{-1}. The scintillation pattern then is dominated by the declining velocity of CME material, 268 ± 42 km s^{-1} between 07:40 and 09:30, and 154 ± 19 km s^{-1} between 09:40 and 12:00. On the other hand, the fast streams display an acceleration progress, $725 \pm 25 \sim 1106 \pm 50$ km s^{-1} obtained from Ys-Hh, $626 \pm 20 \sim 848 \pm 31$ km s^{-1} from Mc-Hh.

The v_{tan} reverses its direction in our measurements, -514 ± 119 km s^{-1} equatorward before 09:30, 84 ± 9 km s^{-1} poleward between 10:00 and 10:30; -290 ± 70 km s^{-1} equatorward between 11:30 and 12:00, and 242 ± 107 km s^{-1} poleward between 12:30 and 13:00.

The oscillation of v_{tan} exhibits large-scale wavelike motions. The direction of v_{tan} turns around between poleward and equatorward, with the wave period of about 2 hr, and a propagation speed in the range of $60 \sim 600$ km s^{-1}. The oscillation of the solar wind complies with the properties of the streamer waves, which is a decaying oscillation of the streamer after the CME passage (Chen et al. 2010; Decraemer

et al. 2020). Chen et al. (2010) and Decraemer et al. (2020) identify the streamer wave in the bright streamer belts from LASCO. The high density sensitivity and spatial resolution of our method enables to find the streamer waves near the north pole of the Sun; a much dimmer area.

Comparing with the CME, where the lag and velocity can be obtained in all the baselines, the propagation of the fast stream is superradial and highly anisotropic. From Figure 6, the fast irregularities stretch out optimally along Hh-Ys, suboptimally along Hh-Mc, and with nonsignificant propagation along Hh-Zc. It means the fast stream has a field-aligned anisotropy along the direction of Hh-Ys. In Appendix Figures 8 and 9, the Ys, Mc, and Zc are different in the tangential direction. Ys is ~ 800 km equatorward off Hh-Mc, and Zc is ~ 1400 km poleward off Hh-Mc. Due to the ~ 2200 km deviation between Zc and Ys in the tangential, the field-aligned anisotropy of the fast stream makes it undetectable along Zc-Hh.

The field-aligned anisotropy of the density fluctuations was also found in the angular broadening data from the Very Large Array (Armstrong et al. 1990; Grail et al. 1996). Harmon & Coles (2005) model the radio scattering and scintillation in the inner solar wind with the oblique Alfvén/ion cyclotron waves. It says the intensity scintillation (IPS) velocities show characteristics consistent with the Alfvén wave dispersion relation. These characteristics include high field-aligned velocity spreads and low perpendicular velocity spreads. It is possible that the field-aligned fast stream measured here is attributed to the effect from Alfvén waves, which propagates in the direction of the magnetic field. It is worthwhile to mention that the cross-correlation analysis presented here could be performed with Faraday rotation fluctuations to detect these magnetic field fluctuations as well as calculating the wave power contained within these fluctuations (Kooi et al. 2017, 2022).

According to the data from Advanced Composition Explorer satellite (ACE)[20], the CME on October 9 is Earth-directed with the Sun–Earth transporting velocity of 620 km s^{-1}. As an important supplement, we measure the velocity of the CME at 2.62 Rs near the north pole of the Sun. The velocity of the CME front measured in the Letter is consistent with ACE, and we also find the CME deflecting to the ecliptic plane before 09:30.

---

[20] http://www.srl.caltech.edu/ACE/ASC/DATA/level3/icmetable2.htm

The solar wind velocity measurement in this study has a rigorous requirement on the projected baseline directions formed by the radio telescopes. At least four telescopes are required to provide the special distribution. We are able to measure the radial velocity of the solar wind because the Hh related baselines cover a broad range in the projected radial distances, finding the streamer wave because Zc-Mc, Mc-Ys, and Zc-Ys cover a broad range in latitudinal distances, but a comparatively short range in radial distance, and finding the field-aligned fast stream because it happened to be highly anisotropic along Hh-Ys. The IPS or FF power spectra analysis of spacecraft signals could also be used to infer the solar wind velocity in the corona (Imamura et al. 2014; Wexler et al. 2020). These methods require only one telescope. However, the IPS focuses on the short-period waves around the Fresnel frequency. We can detect the field-aligned density irregularities caused by the propagation of Alfvén waves with a longer period of 100–500 s. Wexler et al. (2019, 2020) adopted the electron density model in their FF analysis, whereas, it is difficult for the model to depict the instantaneous variations of the electron density in the case of the CME. We should combine the advantages of different methods to study the solar wind velocity in the future.

This work is an in-beam observation of a satellite constellation: TIW and MEX. Kooi et al. (2022) referred to the fact that satellite constellations would provide multiple, closely spaced ray paths to detect the solar corona. In this work, the CNR of MEX is strong enough to study the intensity fluctuations. We prepare to compare the multistation cross-correlation method with the IPS method in the following work.

4. Conclusions

With the reasonable distribution of VLBI radio telescopes, we first visually identify the drift of the scintillation patterns along the projected baselines in the radio band at the sky plane. Combing the visual frequency spikes and the cross-correlation analysis, we have detected the variation of the solar wind velocity during a CME passage at high temporal and spatial resolutions. The oscillation of tangential velocity v_{tan} confirms the detection of a streamer wave, which is usually found in bright streamer belts. At the tail end of the CME, we detect the field-aligned fast flow possibly relating to the Alfvén waves. The detailed physical interpretations of the oscillation and deceleration of the CME, as well as the field-aligned fast density fluctuations are still in research.

The FF observations of spacecraft by radio telescopes provide a unique source to characterize the nascent dynamic solar wind structure. Besides the TIW and MEX, some other deep space spacecraft, e.g., the BepiColombo and the Mars Reconnaissance Orbiter, have high quality beacons as well. We hope to further connect the radio and spacecraft to study the challenging inner solar wind in the future.

Appendix
The Projected Baselines

To study the propagation of solar wind, we have projected the baselines between the station pairs onto the sky plane in heliographic coordinates, then calculated the components in the radial, latitudinal, and longitudinal directions from the Sun. The point of closest approach of the LOS to the Sun is referred to as the projected P point (i.e., impact parameter). The Carrington longitude of P points is 258°, where the longitudinal components of all the projected baselines are usually less than 200 km; therefore we only focus on the radial and latitudinal (usually called tangential in IPS) distance difference between the station pairs; see Figure 8. The reference radial direction is along the heliocenter and Hh. The tangential direction is pointing to the north pole of the Sun. The projected baselines between Ys-Hh and Mc-Hh cover a broad range in radial distances, but a comparatively short range in latitudinal distance. In addition, the baselines between Bd, Zc, Mc, Ys are sensitive in the latitudinal direction. The latitudinal components between Bd-Zc, Zc-Mc, and Mc-Ys are about 2500, 1200, and 800 km, respectively. Meanwhile, the radial components between these station pairs are less than 400 km. Figure 9 consists of the geometric diagrams of projected
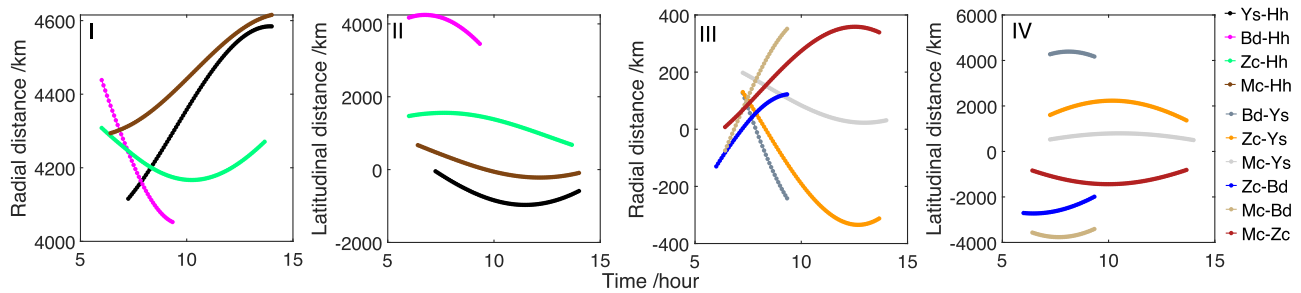
Ma et al.

Figure 8. The projected radial and latitudinal distance. ((I)–(II)). Radial and latitudinal distance at Ys-Hh, Bd-Hh, Zc-Hh, and Mc-Hh. ((III)–(IV)). Radial and latitudinal distance at Bd-Ys, Zc-Ys, Mc-Ys, Zc-Bd, Mc-Bd, and Mc-Zc.
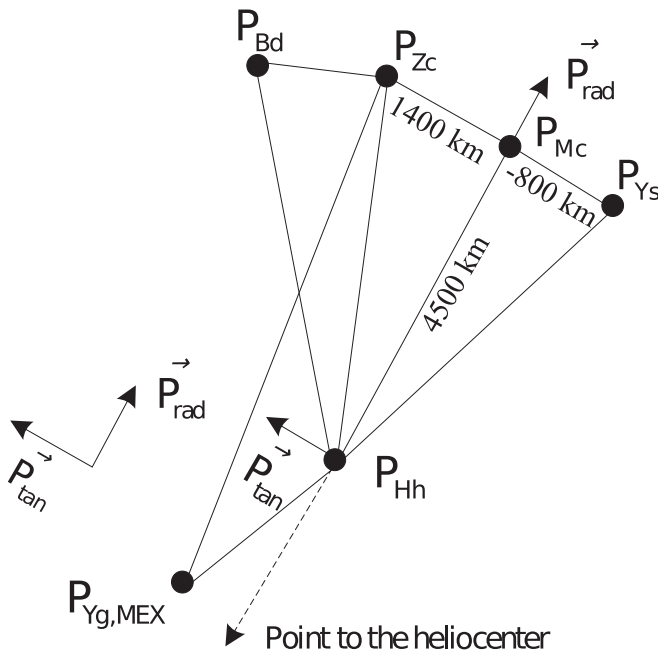

Figure 9. The geometric diagrams of P points in the sky plane on October 9. The distances are marked at UTC 11:00. $P_{Yg,MEX}$ is the P point closest to the Sun from the LOS between MEX and Yg. Other P points are the closest point to the Sun from TIW to the antennas.

baselines in the sky plane. At UTC 11:00, Hh-Mc is aligning the radial direction when the tangential distance between Hh and Mc is zero. We marked the distance scales between Hh, Mc, Ys, and Zc at this moment. The Hh or Yg related baselines are sensitive to the radial direction. The radial solar wind will arrive P_{Yg} first, then P_{Hh}, at the last other P points.

ORCID iDs

Maoli Ma https://orcid.org/0000-0003-2762-1707
Guifré Molera Calvés https://orcid.org/0000-0001-8819-0651

Giuseppe Cimò https://orcid.org/0000-0002-1167-7565
Ming Xiong https://orcid.org/0000-0001-9427-7366
Chuanpeng Hou https://orcid.org/0000-0001-7205-2449
De Wu https://orcid.org/0000-0002-1462-395X
Zhichao Wang https://orcid.org/0000-0001-9234-3921
Javier González https://orcid.org/0000-0001-8689-9835
Andrey Mikhailov https://orcid.org/0000-0002-3355-2261
Giuseppe Maccaferri https://orcid.org/0000-0002-1482-708X

References

Adhikari, L., Zank, G. P., & Zhao, L.-L. 2020, ApJ, 901, 102
Armstrong, J., Coles, W., Kojima, M., & Rickett, B. 1990, ApJ, 358, 685
Bale, S. D., Badman, S. T., Bonnell, J. W., et al. 2019, Natur, 576, 237
Brueckner, G. E., Howard, R. A., Koomen, M. J., et al. 1995, SoPh, 162, 357
Chen, Y., Song, H. Q., Li, B., et al. 2010, ApJ, 714, 644
Decraemer, B., Zhukov, A. N., & Van Doorsselaere, T. 2020, ApJ, 893, 78
Domingo, V., Fleck, B., & Poland, A. I. 1995, SoPh, 162, 1
Efimov, A. I., Lukanina, L. A., Chashei, I. V., et al. 2018, CosRe, 56, 405
Fox, N. J., Velli, M. C., Bale, S. D., et al. 2016, SSRv, 204, 7
Grail, R. R., Coles, W. A., Klinglesmith, M. T., et al. 1996, Natur, 379, 429
Harmon, J. K., & Coles, W. A. 2005, JGRA, 110, 1
He, J., Zhu, X., Yang, L., et al. 2021, ApJL, 913, L14
Imamura, T., Tokumaru, M., Isobe, H., et al. 2014, ApJ, 788, 117
Kooi, J. E., Fischer, P. D., Buffo, J. J., & Spangler, S. R. 2017, SoPh, 292, 56
Kooi, J. E., Wexler, D. B., Jensen, E. A., et al. 2022, FrASS, 9, 1
Ma, M., Calvés, G. M., Cimò, G., et al. 2021a, AJ, 162, 141
Ma, M., Li, P., Tong, F., et al. 2021b, MeScT, 32, 105022
Molera Calvés, G., Kallio, E., Cimo, G., et al. 2017, SpWea, 15, 1523
Molera Calvés, G., Pogrebenko, S. V., Wagner, J. F., et al. 2021, PASA, 38, e065
Patzold, M., Hahn, M., Tellmann, S., et al. 2012, SoPh, 279, 127
Patzold, M., Hausler, B., Tyler, G. L., et al. 2016, P&SS, 127, 44
Schmidt, R. 2003, AcAau, 52, 197
Wexler, D., Imamura, T., Efimov, A., et al. 2020, SoPh, 295, 8
Wexler, D. B., Hollweg, J. V., Efimov, A. I., et al. 2019, ApJ, 871, 202
Zhang, R., Geng, Y., Sun, Z., & Li, D. 2022, Acta Aeronaut. Astronaut. Sin., 43, 626689
Zheng, W., Ma, M., & Wang, W. 2013, Yuhang Xuebao/J. Astronaut., 34, 1462